Available online at www.sciencedirect.com

ScienceDirect

Geochimica et Cosmochimica Acta 271 (2020) 78–95

Geochimica et Cosmochimica Acta

www.elsevier.com/locate/gca

Calibrating equilibrium Fe isotope fractionation factors between magnetite, garnet, amphibole, and biotite

Hui Ye [a], Changzhi Wu [a], Matthew J. Brzozowski [a], Tao Yang [a], Xiangping Zha [b], Shugao Zhao [a], Bingfei Gao [a], Weiqiang Li [a,*]

[a] *State Key Laboratory for Mineral Deposits Research, School of Earth Sciences and Engineering, Nanjing University, Nanjing 210023, China*
[b] *CAS Key Laboratory of Crust-Mantle Materials and Environments, School of Earth and Space Sciences, University of Science and Technology of China, Hefei 230026, China*

Received 30 July 2019; accepted in revised form 11 December 2019; Available online 19 December 2019

Abstract

Equilibrium isotope fractionation factors are the basis for application of stable isotopes in geological studies. Experimental calibration and theoretical calculations have been employed to determine Fe isotope fractionation factors for a variety of minerals, however, these methods have their limitations. An alternative approach to calibrating inter-mineral Fe isotope fractionation factors is to use well-characterized geological samples; this approach has unique advantages over the other methods including attainment of equilibrium at relatively low temperatures. In this study, we investigated the Fe isotope composition of magnetite (Mt), garnet (Grt), amphibole (Amp) and biotite (Bt) from the metamorphosed Yingshan iron formation in South China. Two independent geothermometers, quartz–magnetite oxygen isotope and amphibole–garnet–biotite Fe–Mg exchange geothermometers, give a consistent metamorphic temperature of 538 ± 39 °C. The Fe isotope composition of the different Fe-bearing minerals is highly variable in different ironstone samples, with δ^{56}Fe values (relative to IRMM-014) ranging from −0.23 to +0.37‰ in magnetite, −0.44 to +0.09‰ in amphibole, −0.78 to +0.02‰ in garnet, and −0.61 to +0.04‰ in biotite. Despite that, the offsets of δ^{56}Fe values for mineral pairs are consistent, implying attainment of equilibrium isotope fraction between these minerals. Inter-mineral Fe isotopic fractionations (±2 standard deviation) measured from the multiple mineral pairs are $\Delta^{56}Fe_{Mt-Grt} = +0.55 \pm 0.08‰$, $\Delta^{56}Fe_{Mt-Amp} = +0.25 \pm 0.06‰$, $\Delta^{56}Fe_{Mt-Bt} = +0.42 \pm 0.11‰$, $\Delta^{56}Fe_{Amp-Grt} = +0.34 \pm 0.15‰$, $\Delta^{56}Fe_{Amp-Bt} = +0.26 \pm 0.04‰$, and $\Delta^{56}Fe_{Bt-Grt} = +0.13 \pm 0.08‰$. Based on the well-defined metamorphic temperature (538 ± 39 °C) and internally consistent inter-mineral fractionation factors, the temperature-dependent functions for equilibrium Fe isotope fractionation between the following mineral pairs are derived:

$10^3 \ln\alpha_{Mt-Grt} = 0.36(\pm0.05) \times 10^6/T^2$, $10^3 \ln\alpha_{Mt-Bt} = 0.28(\pm0.07) \times 10^6/T^2$,

$10^3 \ln\alpha_{Mt-Amp} = 0.16(\pm0.04) \times 10^6/T^2$, $10^3 \ln\alpha_{Amp-Grt} = 0.22(\pm0.10) \times 10^6/T^2$,

$10^3 \ln\alpha_{Amp-Bt} = 0.17(\pm0.03) \times 10^6/T^2$, and $10^3 \ln\alpha_{Bt-Grt} = 0.09(\pm0.05) \times 10^6/T^2$,

where $Fe^{3+}/\Sigma Fe$ ratio is 0.05 ± 0.02 in garnet, 0.29 ± 0.04 in biotite, and 0.24 ± 0.06 in amphibole for the above functions. The equilibrium Fe isotope fractionation factors derived in this study enable estimation of the metamorphic temperature of rocks that contain these mineral pairs, and identification of secondary processes that may have induced disequilibrium Fe isotope distribution in rocks, such as retrograde metamorphism and hydrothermal alteration.

Keywords: Iron isotope; Oxygen isotope; Equilibrium isotope fractionation; Geothermometry; Yingshan BIF; Metamorphism

* Corresponding author.
E-mail address: liweiqiang@nju.edu.cn (W. Li).

https://doi.org/10.1016/j.gca.2019.12.014
0016-7037/

1. INTRODUCTION

Iron is an important multivalent metal in nature, and due to the large Fe isotope fractionation associated with redox reactions, Fe isotopes are a sensitive geochemical tool to study a variety of natural processes at both low and high temperatures (e.g., see reviews by Beard and Johnson, 2004; Johnson et al., 2008; Dauphas et al., 2017). For example, Fe isotopes have been successfully applied to studies of metamorphism (e.g., Li et al., 2013; Li et al., 2016; Zhu et al., 2018), magmatic evolution (e.g., Teng et al., 2008; Heimann et al., 2008; Sossi et al., 2012; Dauphas et al., 2014) and planetary evolution (e.g., Shahar et al., 2016; Sossi et al., 2016). Application of stable isotopes to natural systems requires accurate equilibrium isotope fractionation factors for interpretation of observed isotopic data (e.g., Young et al., 2015; Shahar et al., 2017).

Inter-mineral Fe isotope fractionation factors can be derived from theoretical calculation, experimental calibration, and characterization of natural samples (e.g., Schuessler et al., 2007; Shahar et al., 2008; Dauphas et al., 2012, 2014; Liu et al., 2011; Shahar et al., 2016; Liu et al., 2017; Yang et al., 2019). Theoretical calculations of Fe isotope fractionation factors have been undertaken using different approaches, including derivation from experimental data from Mössbauer spectroscopy (e.g., Polyakov and Mineev, 2000; Polyakov et al., 2007; Polyakov and Soultanov, 2011), Nucelar Resonant Inelastic X-ray Scattering (NRIXS) (e.g., Polyakov et al., 2007; Polyakov, 2009; Polyakov and Soultanov, 2011; Dauphas et al., 2012, 2014; Roskosz et al., 2015; Shahar et al., 2016; Liu et al., 2017; Yang et al., 2019), and *ab initio* calculation using quantum mechanics (e.g., Anbar et al., 2005; Domagal-Goldman and Kubicki, 2008; Hill and Schauble, 2008; Ottonello and Zuccolini, 2009; Rustad and Dixon, 2009; Fujii et al., 2014; Blanchard et al., 2009, 2015). The accuracy of calculated Fe isotope fractionation factors is limited by the quality of spectroscopic data (Mössbauer or NRIXS) (Polyakov et al., 2007 and references therein; Dauphas et al., 2014), as well as the necessary simplifications in quantum mechanics models for calculation of reduced partition coefficient factors (Blanchard et al., 2017). It is, therefore, not uncommon for inconsistencies to exist between the Fe isotope fractionation factors calculated in different studies (Dauphas et al., 2012, 2014, 2017; Polyakov and Mineev, 2000; Polyakov et al., 2007; Roskosz et al., 2015).

Another approach for obtaining Fe isotope fractionation factors is to conduct experiments under controlled laboratory conditions (Schuessler et al., 2007; Shahar et al., 2008, 2016; Beard et al., 2010; Frierdich et al., 2014; Sossi and O'Neill, 2017). Although considered as the 'gold standard' for determining isotope fractionation factors, this approach is limited by the balance between reaction rate and isotope fractionation, both of which are temperature dependent. Although Fe isotope fractionation is greater at lower temperatures and is thus preferable from an analytical standpoint (Young et al., 2015), isotope exchange is slower, making it challenging to achieve isotope equilibrium (Shahar et al., 2017). Moreover, kinetic isotope effects need to be evaluated for reactions at low temperatures prior to any attempt of calibrating equilibrium isotope fractionations (O'Neil, 1986). In contrast to this scenario, under high-temperature conditions, where exchange rates are high and kinetic isotope effects could be reduced, isotope fractionation factors are smaller and difficult to resolve. Furthermore, experimental determination of isotope fractionation at high temperatures requires a combination of expertise in high P–T experimentation, high-precision isotope mass spectrometry, and in many cases the ability to handle enriched isotope tracers (Shahar et al., 2017). Consequently, only few high-temperature experiments have been done to characterize inter-mineral Fe isotope fractionation; these were generally restricted to mineral pairs with large Fe isotope fractionations (e.g., Shahar et al., 2008; Sossi and O'Neil, 2017).

The third approach for obtaining isotope fractionation factors is to analyze co-existing mineral pairs in natural rocks (e.g., Li et al., 2011; Li et al., 2016). The greatest advantage of this approach is that geological processes last a long time, exceeding the time of laboratory experiments by many orders of magnitude. Therefore, minerals within a rock are likely to have reached equilibrium even at lower temperatures. There are several challenges using this approach, however, including (1) confirmation of isotopic equilibrium or disequilibrium, (2) constraining the physicochemical conditions (i.e., P–T–fO_2) for the measured isotope fractionation factors, and (3) identification of the main geological processes that imposed isotope equilibrium and the secondary processes that broke isotope equilibrium in rocks. Because of these issues, successful case studies of inter-mineral Fe isotope fractionation calibration based on rocks are scarce and generally limited to igneous rocks and eclogites (Huang et al., 2011; Sossi et al., 2012; Li et al., 2016).

Magnetite, garnet, amphibole, and biotite are common Fe-bearing rock-forming minerals. Yet, reports of inter-mineral Fe isotope fractionation data with well-constrained equilibrium temperatures for these minerals are scarce in the literature, except for an experimental study on Fe isotope fractionation between magnetite and garnet (Sossi and O'Neil, 2017). The Yingshan banded iron formation in South China underwent amphibolite-facies metamorphism and contains abundant co-existing magnetite, garnet, amphibole, and biotite, providing a great opportunity for calibrating inter-mineral Fe isotope fractionation for these minerals. Based on detailed petrographic observations, we collected high-precision Fe isotope, O isotope, and major–element chemistry data of magnetite, garnet, amphibole, and biotite from a suite of samples from the Yingshan banded iron formation. Multiple criteria were used to rigorously test the attainment of Fe isotope equilibrium between the four minerals, with equilibration temperatures determined using two independent geothermometers. The results not only enable us to derive equilibrium Fe isotope fractionation factors for the four minerals, but also to identify post-metamorphic processes that modified the Fe isotope composition of the ironstone samples.

2. GEOLOGICAL BACKGROUND AND SAMPLES

The Yingshan banded iron formation (YBIF) is a newly identified banded iron formation of Neoarchean age in the northeast of Yangtze Craton (Ye et al., 2017). The YBIF is hosted by the metamorphosed Neoarchean–Paleoprotero zoic Feidong Group, which is part of the southern Zhangbaling zone in the Dabie–Sulu orogenic belt. The Dabie–Sulu orogenic belt (Fig. 1b), formed by the collision of the Yangtze and North China cratons in the Triassic (Zheng et al., 2019), is one of the largest ultrahigh-pressure (UHP) metamorphic terrains on Earth (e.g., Zheng, 2012). After subduction to subarc depths, metamorphic rocks in the Dabie–Sulu orogenic belt were exhumed to crustal levels, forming five metamorphic zones (Zhang et al., 1995; Zheng et al., 2005), which are, form north to south, the high-P blueshist facies belt, the high-P amphibolite (±eclogite) zone, the UHP eclogite facies zone, the migmatite to granulite facies zone, and the greenschist facies belt (Fig. 1b). The YBIF occurs within the volcanic–sedimentary successions of the Neoarchean–Paleoproterozoic Feidong Group in the amphibolite facies zone. It is composed of three banded orebodies that extend northeast–southwest for over 20 km, with an average thickness of over 10 m. The YBIF is characterized by a banded structure of alternating Si- and Fe-rich layers of variable thickness (meter- to sub-millimeter) (Ye et al., 2017). The YBIF has a mineral assemblage of amphibole–biotite–garnet–quartz–magnetite, indicative of amphibolite-facies metamorphism (Yardley, 1989). This was confirmed by its metamorphic temperature of 524 °C based on amphibolite–garnet Fe–Mg exchange thermometry (Shi et al., 2009).

Sixteen BIF samples were collected from the orebodies of the YBIF (Fig. 1); the whole-rock Fe isotope compositions for these samples have previously been reported (Ye et al., 2017). Most of the samples are unaltered (Fig. 2), however, detailed petrographic observations revealed that amphibole in some samples were affected by post-metamorphic processes. In some samples (YS-32, YS-34) (Fig. 2e, f; Table 1), the amphibole grains have been partly replaced by chlorite (Supplementary Fig. S3, Fig. S4; Table S3), implying interaction with hydrothermal fluids; this type of altered amphibole is defined as A-Amp. In some other samples (YS-33, YS-50, YS-52), amphibole was replaced by chlorite (Fig. 2g, h), but the chlorite retains the morphology and optical extinction orientation of the amphibole (Fig. 2g), implying a retrograde metamorphic origin; this type of metamorphosed amphibole is defined as R-Amp (Fig. 2g, h; Supplementary Fig. S3, Fig. S4; Table S3). Apart from A- and R-Amp, the Fe-bearing minerals in the samples (Amp + Grt + Qz + Mt + Bt) are fresh (Fig. 2) and compositionally homogeneous with respect to their major elements (Fig. 3).

3. ANALYTICAL METHODS

3.1. Sample preparation

Polished thin sections were made from all 16 samples, with the remaining material crushed to 50–100 mesh for

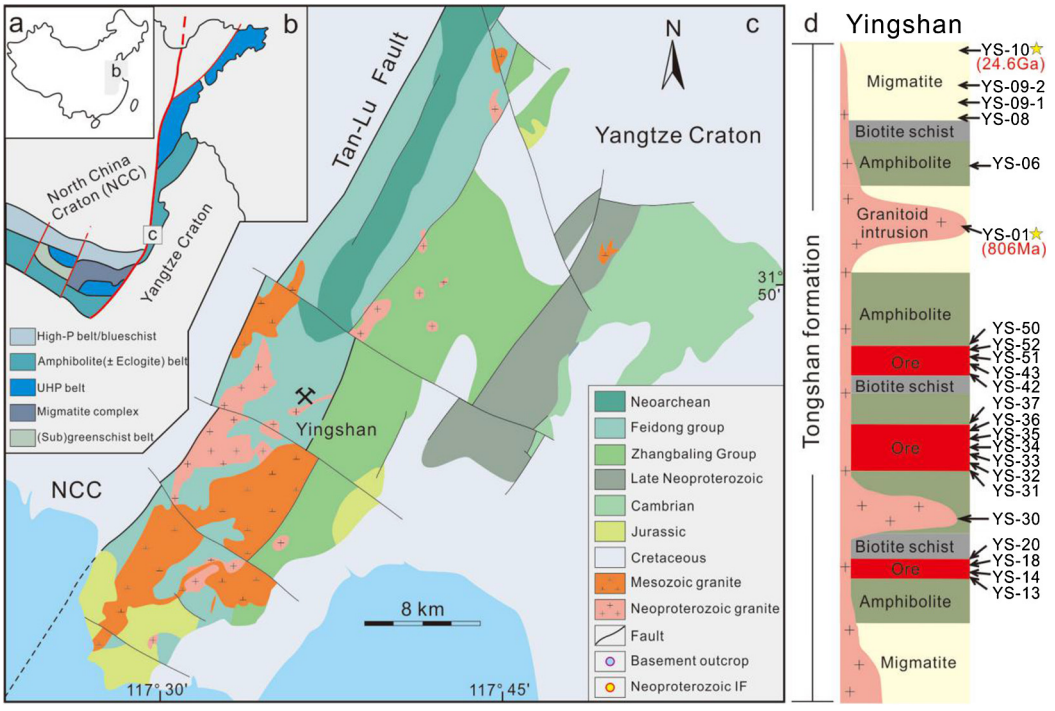

Fig. 1. (a) Location of the Dabie-Sulu orgen in central-east China. (b) Simplified geological map of the Dabie-Sulu orgen in central-east China. (c) Simplified geological map of the Yingshan banded iron formation (YBIF). (d) Stratigraphic column of the YBIF showing sampling point (arrow) and zircon U-Pb age (star). (modified after Ye et al., 2017).

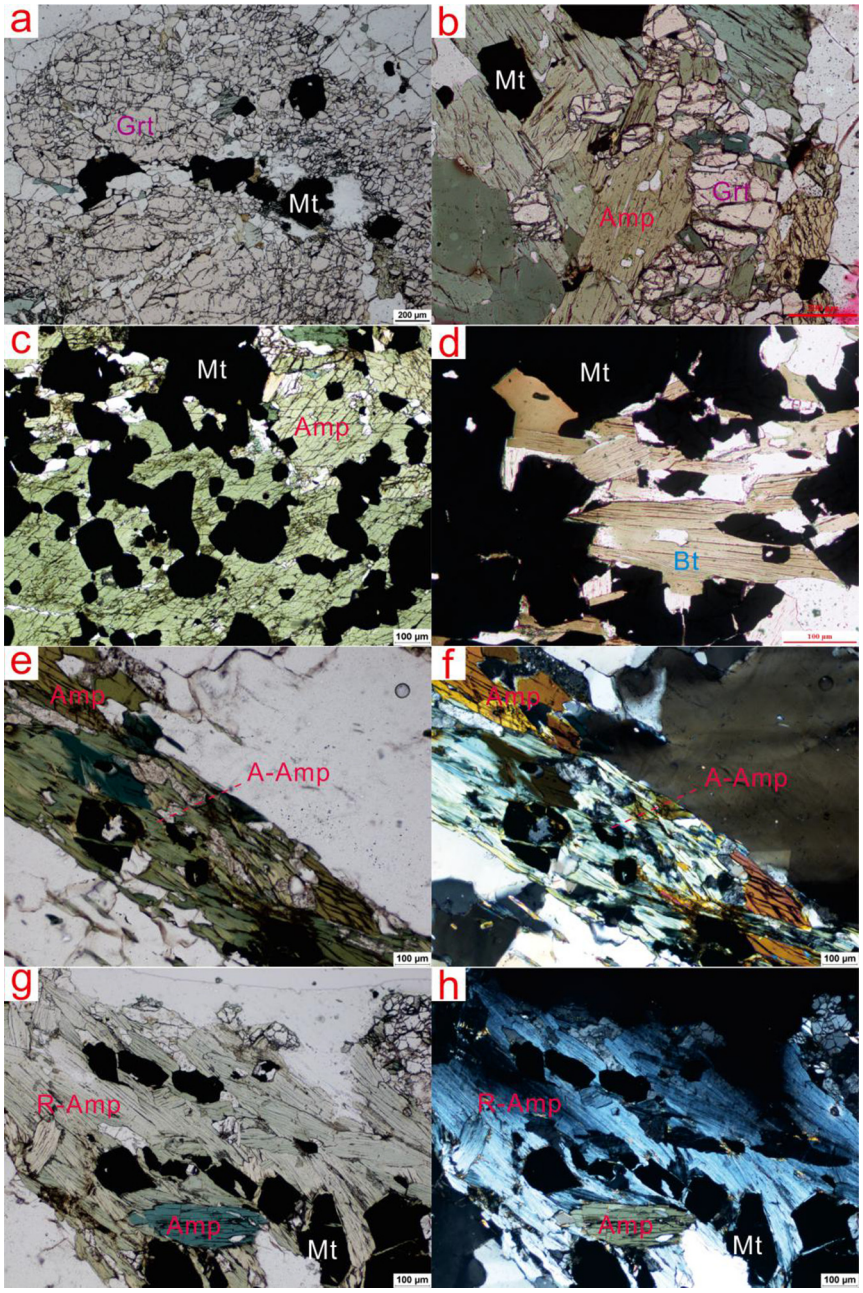

Fig. 2. Photomicrographs of co-existing minerals from the YBIF. (a–d). Unaltered and euhedral co-existing magnetite-garnet-amphibolite-biotite assemblages from the YBIF. (e–f) A-Amp (chlorite) in sample YS-34 exhibiting an irregular replacement texture under plane- and cross-polarized light, respectively. (g–h) R-Amp (chlorite) in sample YS-33 that has the same shape, color, and cleavage as amphibole under plane-polarized light, but has interference colors typical of chlorite. Mt, Magnetite; Grt, Garnet; Amp, Amphibole; Bt, Biotite; A-Amp, Altered amphibole; R-Amp, Retrograde metamorphic amphibole.

mineral separation. The Fe-bearing minerals were initially separated using magnetic and density–gravity methods, and then handpicked and visually inspected under a binocular microscope. The purity of the separates was estimated to be >99%. The minerals were repeatedly rinsed in deionized water before digestion and chemical analysis. For Mössbauer spectroscopy, each Fe-bearing mineral separate sample was crushed to a fine power (200 mesh) using an agate mortar and pestle.

3.2. Micro-X-ray fluorescence mapping

Elemental distribution in polished thin sections was characterized by micro-X-ray fluorescence (μ-XRF) spectrometry using an IXRF ATLAS® μ-XRF scanner at the State Key Laboratory for Mineral Deposits Research, School of Earth Sciences and Engineering, Nanjing University. The instrument is equipped with a Rh-target microbeam X-ray source and a 150 mm^2 SDD

Table 1
The Fe and O isotope compositions, and $Fe^{3+}/\sum Fe$ ratio of co-existing minerals in Yingshan BIF samples.

Sample ID	Rock type	Minerals	$\delta^{56}Fe$	2SE/SD	$\delta^{57}Fe$	2SE/SD	N	$\delta^{18}O$	2SD	N	$Fe^{3+}/\sum Fe(\%)$
YS-13	BIF	Mt	−0.1	0	−0.13	0	2	3.68	0.01	2	
		Grt	−0.62	0.02	−0.82	0.04	1				6.3
		Bt	−0.48	0.02	−0.63	0.05	3				30.3
		Qz						13.69	0.08	2	
YS-14	BIF	Mt	−0.16	0.01	−0.22	0.04	2	5.45	0.47	2	
		Amp	−0.44	0.01	−0.64	0.16	2				23.3
		Qz						14.7	0.2	2	
YS-18	BIF	Mt	0.32	0	0.45	0.17	2	3.82	0.31	2	
		Grt	−0.2	0.1	−0.3	0.15	3				5.4
		Bt	−0.12	0.03	−0.17	0.04	3				31.3
		Qz						14.09	1	2	
YS-20	BIF	Mt	0.23	0.07	0.37	0.07	2	3.85	0.59	2	
		Grt	−0.31	0.11	−0.41	0.15	3				5.0
		Bt	−0.15	0.03	−0.21	0.06	3				26.9
		Qz						13.91	0.37	2	
YS-31	BIF	Amp	−0.3	0.05	−0.41	0.25	2	5.04	0.23	2	18.1
		Bt	−0.55	0.03	−0.71	0.05	3				
		Qz						13.94	0.21	2	
YS-32	BIF	Mt	0	0.05	0	0.13	2	3.86	0.24	2	
		A-Amp	−0.1	0.06	−0.13	0.04	2				19.9
		Qz						13.22	0.38	2	
YS-33	BIF	Mt	0.21	0.06	0.37	0.05	2	4.85	0.24	2	
		R-Amp	−0.21	0.11	−0.3	0.14	2				22.2
		Qz						14.45	0.57	2	
YS-34	BIF	Mt	0.08	0.02	0.06	0.22	2	4.34	0.59	2	
		A-Amp	0.09	0.06	0.21	0.05	2				32.5
		Bt	−0.4	0.07	−0.59	0.08	2				27.0
		Qz						11.73	0.42	2	
YS-35	BIF	Mt	−0.23	0.1	−0.25	0.03	2	3.76	0.57	2	
		Grt	−0.78	0.02	−1.07	0.03	2				4.9
		Bt	−0.61	0.03	−0.91	0.03	2				29.1
		Qz						13.71	0.01	2	
YS-36	BIF	Mt	−0.14	0.03	−0.17	0.05	1	3.9	0.23	2	
		Amp	−0.36	0.05	−0.51	0.08	2				26.7
		Grt	−0.67	0.03	−0.89	0.04	3				6.4
		Bt	−0.59	0.03	−0.8	0.02	2				26.0
		Qz						13.58	0.04	2	
YS-37	BIF	Mt	0.3	0.03	0.4	0.05	1				
		Amp	0.04	0.09	0.07	0.01	2				26.8
		Grt	−0.25	0.08	−0.35	0.05	3				6.3
		Qz									
YS-42	BIF	Mt	−0.12	0.02	−0.2	0.05	1	4.82	0.23	2	
		Amp	−0.33	0.08	−0.55	0.02	2				20.0
		Grt	−0.76	0.05	−1.05	0.07	3				3.0
		Bt	−0.6	0.04	−0.85	0.05	3				30.0
		Qz						14.75	0.07	2	
YS-43	BIF	Mt	−0.18	0.03	−0.12	0.07	1	5.5	0.08		
		Grt	−0.75	0.06	−1.05	0.05	3				6.3
		Qz						14.86	0.25	2	
YS-50	BIF	Mt	0.27	0.03	0.44	0.01	2	3.89	0.06		
		R-Amp	−0.16	0.06	−0.16	0	2				25.4
		Bt	−0.18	0.05	−0.23	0.02	3				31.3
		Qz						12.68	0.44	2	
YS-51	BIF	Mt	−0.05	0.09	−0.05	0.05	2	5.25	0.3	2	
		Amp	−0.31	0.07	−0.4	0.11	2				21.1
		Qz						14.06	0.61	2	
YS-52	BIF	Mt	0.37	0.1	0.54	0.05	2	3.95	0.3	2	
		R-Amp	−0.09	0.05	−0.08	0.2	2				26.2
		Bt	0.04	0.02	0.05	0.05	1				31.6
		Qz						13.86	0.23	2	

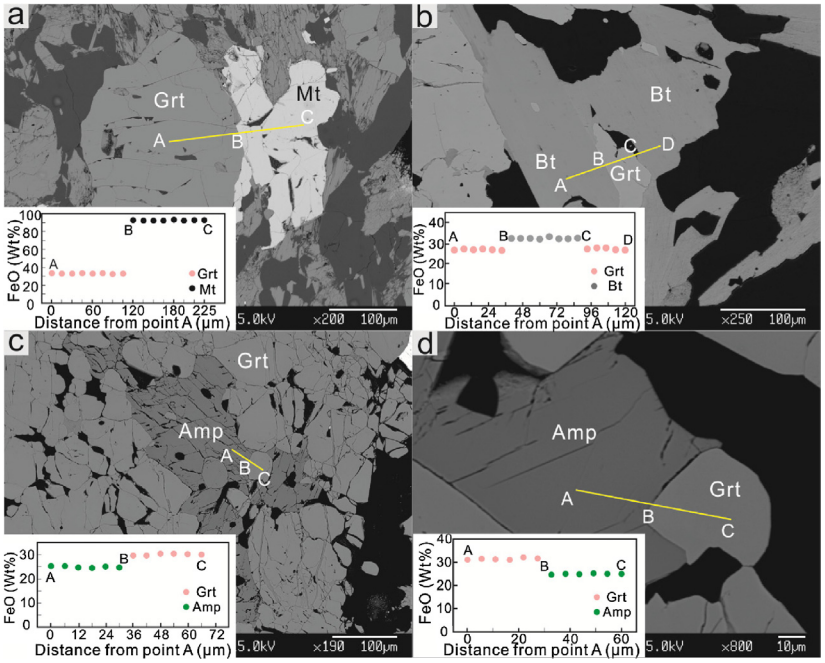

Fig. 3. Backscatter electron images and FeO contents of representative minerals from the YBIF. (a) profile analysis across a garnet-magnetite boundary (sample YS-18), (b) profile analysis across a garnet grain surrounded by biotite (sample YS-13), and (c–d) profile analysis across two amphibole-garnet boundaries (sample YS-37). The co-existing minerals show chemical homogeneity in FeO_T profile of EMPA and under BSE images.

energy-dispersive X-ray detector. For elemental mapping, the micro X-ray source was operated at 50 kV and 500 μA, motor steps of 50 μm in the X–Y direction, a spot size of 10 μm, and a collection time of 10 ms for each pixel. Spatially-resolved energy-dispersive spectroscopic data were processed with the μ-XRF Iridium software to generate semi-quantitative elemental distribution maps. The ImagePy software (Wang et al., 2018) was used to quantify the relative abundance of the different Fe-bearing minerals in each polished section (Fig. S2; Supplementary Table S4).

3.3. Electron microprobe analysis

The major–minor element composition of magnetite, amphibole, garnet and biotite in the polished sections was measured using a JEOL 8100 electron probe microanalyzer (EMPA) at the State Key Laboratory for Mineral Deposits Research, School of Earth Sciences and Engineering, Nanjing University. The instrument was operated at an accelerating voltage of 15 kV, a beam current of 20 nA, and a spot size of 1 μm. A set of natural and synthetic mineral and metal standards were used for calibration. The raw data was reduced using the ZAF correction procedure.

3.4. Mössbauer spectroscopy

Mössbauer spectroscopic analyses were performed on a Bench MB-500 Mössbauer spectrometer at the Key Laboratory of Petroleum Resources Research, Institute of Geology and Geophysics, Chinese Academy of Sciences following an established method (Ma et al., 2018). The instrument was operated using a γ-ray source of 0.927 GBq 57Co/Rh at room-temperature (~297 K). About 30–60 mg of powdered mineral separate was gently pressed into an iron-free plastic sample holder. Transmission Mössbauer spectra obtained from the instrument were fitted to Lorentzian line shapes with the WinNoroms-for-Igor software (version 6.0) to derive the Fe^{2+}/Fe^{3+} ratios (e.g., Peng et al., 2013). Mössbauer spectrum of an α-Fe foil ($^{57}Fe > 99.85\%$) was used to calibrate the center position of the spectrum and hyperfine parameters.

3.5. Oxygen isotope analysis

The oxygen isotope composition of quartz and magnetite separates was measured at the CAS Key Laboratory of Crust-Mantle Materials and Environments, University of Science and Technology of China, Hefei. Details regarding instrumental conditions and data acquisition protocols were described by Zheng et al. (2002). Briefly, oxygen was released from the minerals by laser fluorination using a 25 W MIR-10 CO_2 laser. After purification, O_2 was transferred to a Delta + mass spectrometer for $^{18}O/^{16}O$ measurement. The O isotope data are reported as parts per thousand (‰) relative to standard VSMOW in $\delta^{18}O$ notation. Two reference minerals were measured to ensure data quality: GBW04409 quartz ($\delta^{18}O = 11.1‰$) (Zheng et al., 1998) and the in-house standard 04BXL07 garnet ($\delta^{18}O = 3.7‰$) (Gong et al., 2007). Each mineral was analyzed at least twice. Reproducibility of each reference mineral on a given day was better than ±0.2‰ (2σ) for $\delta^{18}O$.

3.6. Iron isotope analysis

The Fe isotope composition of the iron-bearing minerals was measured at the State Key Laboratory for Mineral Deposits Research, School of Earth Sciences and Engineering, Nanjing University, following the established method that has been reported in detail in Ye et al., 2017 and Du et al., 2017. Ten milligrams of mineral separate were digested in 4 mL of a 2:1:1 mixture of concentrated HCl–HNO_3–HF in a tightly capped 7 mL Teflon beaker, which was heated at ~130 °C on a hotplate for 2 days. After digestion, the sample was dried and re-dissolved in 2 mL of 6 M HCl, and a small aliquot of the sample stock solution was taken for measurement of total Fe using either spectrophotometry (i.e., Ferrozine method) (Stookey, 1970) or ICP-OES. Based on the Fe concentration data, approximately 100 μg of Fe was taken from the sample stock solution and purified by anion exchange chromatography using 0.2 mL Bio-Rad AG MP-1 resin (Ye et al., 2017; Du et al., 2017). After purification, the Fe solution was diluted to 2 ppm for isotope measurement on a Thermo Fisher Scientific Neptune Plus MC–ICP–MS using the standard–sample–standard bracketing routine. The instrument was operated at medium mass resolution and "wet-plasma" mode using a 100 μL/min self-aspirating nebulizer and a glass spray chamber. Iron isotope compositions are reported as $\delta^{56}Fe$ relative to the international standard IRMM-014:

$$\delta^{56}Fe_{sample} = \left[\left(^{56}Fe/^{54}Fe\right)_{sample}/\left(^{56}Fe/^{54}Fe\right)_{IRMM-014} - 1\right] \times 1000(‰) \quad (1)$$

The long-term external reproducibility (2 standard deviation or 2 SD) of the Fe isotope analyses is better than ±0.06‰ for $^{56}Fe/^{54}Fe$ and ±0.16‰ for $^{57}Fe/^{54}Fe$ based on repeat analyses of multiple Fe isotope standard solutions, as well as purified USGS rock standards against an in-house stock solution (Ye et al., 2017; Du et al., 2017).

4. RESULTS

4.1. Mineral chemistry

Compositional profiles reveal that the Fe-bearing minerals are homogeneous within the analytical uncertainly of EPMA, consistent with backscatter electron images (BSE) (Fig. 3, Supplementary Table S2, Table S6). Garnet grains contain high concentrations of FeO_T (31.02–33.88 wt.%) and CaO (5.00–8.36 wt.%), but low concentrations of MgO (0.93–1.69 wt.%) and MnO (1.17–3.43 wt.%) (Supplementary Table S2), suggesting that the garnets from the YBIF are close to the almandine end-member (Supplementary Fig.S1). Amphibole grains also have high concentrations of FeO_T (24.95–25.45 wt.%) and CaO (11.27–11.46 wt.%), but low concentrations of MgO (3.61–3.97 wt.%) and MnO (0.13–0.16 wt.%), with a $Ca_B > 1.5$ and $Na + K < 0.5$, indicating that they are calcic amphiboles (Supplementary Table S2; Fig.S1) (Leake et al., 1997). Biotite grains have high concentrations of FeO_T (23.86–31.76 wt.%), MgO (4.29–8.51 wt.%), Al_2O_3 (17.04–18.07 wt.%), and K_2O (7.01–9.19 wt.%), but low concentrations of MnO (0.05–0.34 wt.%) and CaO (0.01–0.05 wt.%). Relative to fresh amphiboles, A-Amp and R-Amp are enriched in Al_2O_3 (18.67–19.58 wt.%), FeO_T (32.46–34.6 wt.%), MgO (8.41–10.25 wt.%), and MnO (0.43–0.83 wt.%), but depleted in CaO (0–0.05 wt.%), Na_2O (0.02–0.10 wt.%), and K_2O (0.01–0.46 wt.%), with total major–minor-element contents of less than 90.5 wt.% (Supplementary Table S3); these mineral phases are compositionally similar to chlorite (Supplementary Fig. S3, Fig. S4; Table S3).

The Fe^{2+}/Fe^{3+} ratios of Fe-bearing minerals estimated by EMPA are confirmed by Mössbauer spectroscopy (Table 1; Supplementary Table S1). $Fe^{3+}/\sum Fe$ ratios range from 3.0 to 6.4% (average = 5.5 ± 2.3%, 2SD) for garnet, 26.0 to 31.6% (average = 29.3 ± 4.3%, 2SD) for biotite, and 20.0 to 26.8% (average = 23.6 ± 6.3%, 2SD) for amphibole. In contrast, A-Amp exhibits a large range in $Fe^{3+}/\sum Fe$ (19.9–32.5%), whereas R-Amp exhibits a limited range in $Fe^{3+}/\sum Fe$ (22.2–26.2%) that is similar to and comparable with fresh amphibole (Table 1; Supplementary Table S1).

4.2. Oxygen isotopes

Quartz and magnetite in most samples have relatively uniform $\delta^{18}O$ values ranging from 3.68–5.50‰ and 11.73–14.86‰, respectively (Fig. 4; Fig. 5; Table 1). It is important to note that despite the small, but discernible variations in $\delta^{18}O$ values for both quartz and magnetite in the YBIF samples, the offset in $\delta^{18}O$ values between the two minerals ($\Delta^{18}O_{Mt-Qz}$) is less variable. If the anomalously low $\delta^{18}O$ values of 11.73‰ for the quartz from sample YS-34, which shows considerable replacement of amphibole by chlorite (A-Amp) (Fig. 2e), is ignored, the offset is 9.56‰ ± 0.99‰ (2SD, n = 14; Table 2).

4.3. Iron isotopes

The $\delta^{56}Fe$ values of the Fe-bearing minerals in the YBIF are highly variable, with a range of 1.25‰. Mineralogy exerts the first-order control on the $\delta^{56}Fe$ values, with magnetite having the highest $\delta^{56}Fe$ values (−0.23 to +0.37‰) and garnet having the lowest values (−0.78 to −0.20‰). The range of $\delta^{56}Fe$ values for amphibole and biotite are −0.44 to +0.04‰ and −0.61 to +0.04‰, respectively. Accordingly, in order of heavy Fe isotope enrichment, the minerals are magnetite > amphibole > biotite > garnet, consistent with previous studies (e.g., Li et al., 2016; Sossi and O'Neil, 2017). The $\delta^{56}Fe$ values of A-Amp and R-Amp vary from −0.10 to +0.09‰ and −0.09 to −0.21‰, respectively (Fig. 4; Fig. 6; Table 1).

We further consider the isotope mass balance of Fe in each of the YBIF samples by calculating the whole-rock Fe isotope composition of each sample using the measured $\delta^{56}Fe$ of each of the Fe-bearing minerals ($\delta^{56}Fe_i$; Fig. 4, Table 1) and the relative mass fraction of Fe in that mineral (C_i) as measured by elemental mapping (Supplement Fig. S2; Table S4):

$$\delta^{56}Fe_{whole-rock} = \sum_{n=1}^{k} C_i \times \delta^{56}Fe_i \quad (2)$$

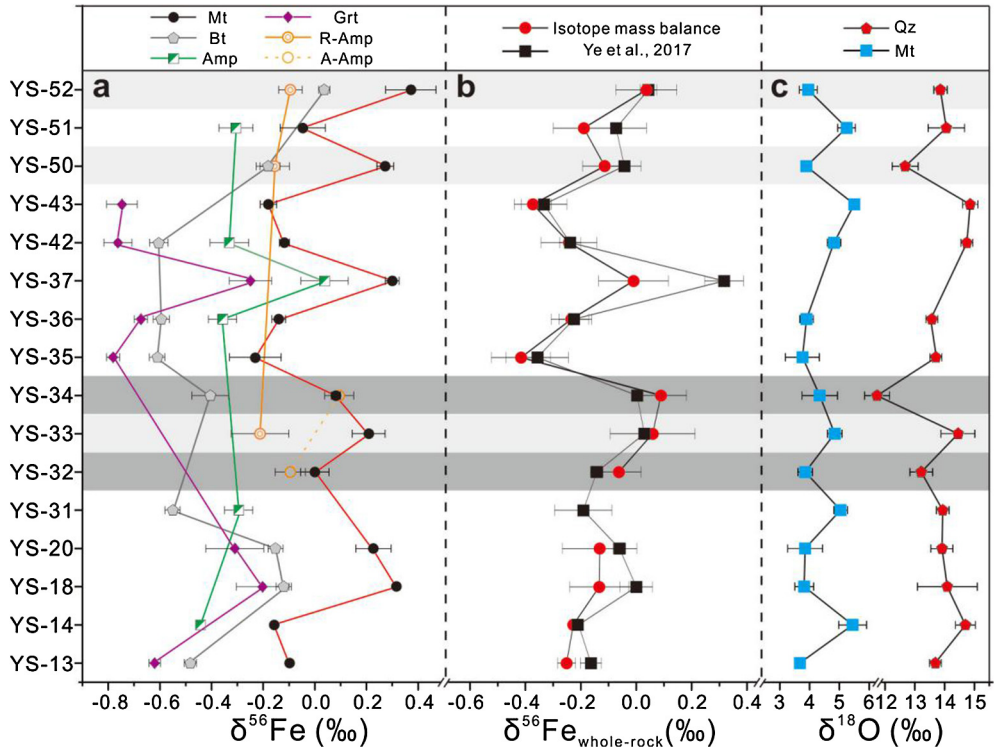

Fig. 4. (a) Fe isotope composition of co-existing Fe-bearing minerals; (b) calculated whole-rock Fe isotope composition of the samples (Supplement Fig. S2; Table S4) and measured values from Ye et al., 2017; (c) O isotope compositions of quartz and magnetite. The dark grey bands represent samples that were hydrothermally altered, whereas the light grey bands represent samples were modified by retrograde metamorphism. Mt, Magnetite; Qz, Quartz; Grt, Garnet; Amp, Amphibole; Bt, Biotite; A-Amp, Altered amphibole; R-Amp, Retrograde metamorphic amphibole.

where k is the total number of coexisting Fe-bearing minerals in the YBIF sample. Despite the highly variable Fe isotope composition of the different minerals in different samples, the modeled bulk $\delta^{56}Fe$ of each individual sample is generally consistent with the $\delta^{56}Fe$ value measured from whole-rock powders (Ye et al., 2017) within analytical uncertainty (Fig. 4b).

Despite the large variation in Fe isotope composition of each mineral, the offsets in $\delta^{56}Fe$ between Fe-bearing mineral pairs are remarkably consistent (Fig. 6; Table 2), with $\Delta^{56}Fe_{Mt-Grt}$ of $0.55 \pm 0.08‰$ (2SD, n = 8), $\Delta^{56}Fe_{Mt-Amp}$ of $0.25 \pm 0.06‰$ (2SD, n = 5), $\Delta^{56}Fe_{Mt-Bt}$ of $0.42 \pm 0.11‰$ (2SD, n = 9), $\Delta^{56}Fe_{Amp-Grt}$ of $0.34 \pm 0.15‰$ (2SD, n = 3), $\Delta^{56}Fe_{Amp-Bt}$ of $0.26 \pm 0.04‰$ (2SD, n = 3) and $\Delta^{56}Fe_{Bt-Grt}$ of $0.13 \pm 0.08‰$ (2SD, n = 6).

5. DISCUSSION

5.1. Temperature of metamorphism

Oxygen isotope thermometry based on mineral pairs has been widely used to constrain the temperature of metamorphism (e.g., Zheng et al., 1998, 2003; Valley, 2001). The quartz–magnetite pair has several distinct advantages for O isotope thermometry, including the large magnitude of inter-mineral isotope fractionation and the uniformity in crystal chemistry of the two minerals (e.g., Zheng, 1995). The quartz–magnetite O isotope thermometer has been successfully applied to unravel the thermal histories of iron formations (e.g., Becker and Clayton, 1976; Li et al., 2013). As illustrated in Fig. 5a, the $\delta^{18}O$ values of magnetite and quartz co-vary in each of the YBIF samples (apart from sample YS-34) and define a constant $\Delta^{18}O_{Qz-Mt}$ value of $9.56 \pm 0.99‰$, suggesting the attainment of O isotope equilibrium between quartz and magnetite. Based on the experimentally calibrated equilibrium O isotope fractionation function between quartz and magnetite ($10^3 \ln\alpha_{Qz-Mt} = 6.29 \times 10^6/T^2$, T in kelvin) (Chiba et al., 1989), the metamorphic temperatures for the YBIF samples are calculated to be 497–581 °C, with an average of 538 ± 39 °C (2 SD).

The experiments by Chiba et al. (1989) were performed at a temperature range of 800–1200 °C and so there is a concern whether this function can be extrapolated to a lower temperature of 500 °C. To assess this, we compiled a comprehensive set of $10^3 \ln\alpha_{Qz-Mt}$ functions based on literature values of beta factors (lnβ) for quartz and magnetite derived by theoretical calculations and experimental calibrations. All $10^3 \ln\alpha_{Qz-Mt}$ functions converge at temperatures over 500 °C (Supplementary Fig. S6; Table S7). The corresponding temperatures calculated using these different $10^3 \ln\alpha_{Qz-Mt}$ functions range from 533 °C to 565 °C, with an average of 546 ± 26 °C (n = 7; 2SD). These are indistinguishable within error to the results calculated using the function of Chiba et al. (1989), attesting to the accuracy of the O isotope thermometry.

Table 2
Inter-mineral O and Fe isotope fractionation for samples of the Yingshan BIF.

Sample	$\Delta^{56}Fe_{Mt\text{-}Grt}$	2SD	$\Delta^{56}Fe_{Mt\text{-}Amp}$	2SD	$\Delta^{56}Fe_{Mt\text{-}Bt}$	2SD	$\Delta^{56}Fe_{Amp\text{-}Grt}$	2SD	$\Delta^{56}Fe_{Amp\text{-}Bt}$	2SD	$\Delta^{56}Fe_{Bt\text{-}Grt}$	2SD	$\Delta^{18}O_{Mt\text{-}Qzt}$	2SD
YS-13	0.52	0.02			0.38	0.02					0.14	0.03	10.02	0.07
YS-14			0.29	0.01									9.26	0.27
YS-18	0.52	0.10			0.44	0.03					0.08	0.11	10.27	0.69
YS-20	0.54	0.13			0.38	0.07					0.16	0.12	10.06	0.22
YS-31									0.26	0.06			8.90	0.01
YS-32													9.36	0.14
YS-33													9.61	0.33
YS-34					0.49	0.07					0.17	0.04	7.39	0.17
YS-35	0.55	0.10			0.38	0.10							9.95	0.55
YS-36	0.53	0.04	0.22	0.06	0.46	0.04	0.32	0.06	0.24	0.06	0.08	0.04	9.68	0.18
YS-37	0.55	0.09	0.26	0.10			0.29	0.12						
YS-42	0.64	0.06	0.21	0.08	0.49	0.04	0.43	0.09	0.27	0.08	0.16	0.06	9.93	0.16
YS-43	0.57	0.07											9.36	0.17
YS-50					0.45	0.06							8.79	0.38
YS-51			0.26	0.11									8.81	0.31
YS-52					0.34	0.10							9.91	0.07
Average	0.55	0.08	0.25	0.06	0.42	0.11	0.34	0.15	0.26	0.04	0.13	0.08	9.56*	0.99*

* Sample YS-34 excluded as an outlier for the calculation.

Thermometry using the partitioning of Fe–Mg between co-existing silicate minerals is another classic tool to study prograde to retrograde metamorphic processes (e.g., Krogh, 1988). Experimental and theoretical studies have demonstrated that under thermodynamic equilibrium, partitioning of Fe^{2+} and Mg^{2+} (D_K) between a range of minerals is strongly temperature dependent (e.g., Ferry and Spear, 1978; Holdaway and Lee, 1977; Ravna, 2000). The accuracy of Fe–Mg exchange thermometry can be affected by uncertainty in the $Fe^{3+}/\sum Fe$ ratio calculated based on EMPA data (e.g., Krogh and Raheim, 1978; Carswell and Zhang, 1999). In this study, Fe^{2+} concentrations in garnet and amphibole were accurately determined using EMPA data in combination with high quality $Fe^{3+}/\sum Fe$ ratios measured by Mössbauer spectroscopy (Supplementary Table S1). The Fe–Mg cation partitioning temperature was calculated using the $T–D_K$ function of Graham and Powell, (1984) and Ravna (2000) for garnet–amphibole pairs; the results range from 539 to 604 °C, with an average of 561 ± 50 °C (2 SD) (Supplementary Table S2). Iron–Mg partitioning temperatures were also calculated using the formula of Holdaway (2000) for garnet–biotite pairs, with temperatures ranging from 523 to 567 °C, with an average of 554 ± 42 °C (2 SD) (Supplementary Table S2).

The uniformity in O isotope equilibration temperatures for 15 of the 16 samples from the YBIF, along with the consistency between temperatures obtained by O isotope thermometry and inter-mineral Fe–Mg exchange thermometry confirm that the YBIF samples experienced amphibolite-facies metamorphism. Our data is also in agreement with Shi et al. (2009), who suggested that the host rocks of the YBIF experienced peak metamorphic temperatures of 524 ± 13 °C. The combination of these two independent thermometers leads to a robust constraint on the metamorphic temperature for the YBIF samples. In the following discussion, we conservatively use the temperature data constrained from the quartz–magnetite O isotope thermometer as it is based on more data (n = 15).

5.2. Attainment of inter-mineral Fe isotope equilibrium

Multiple lines of evidence demonstrate that Fe isotope equilibrium was attained for the samples from the YBIF, including (1) chemical homogeneity within individual mineral grains, (2) consistent inter-mineral Fe isotope fractionation factors despite large inter-sample Fe isotope variations for each mineral, and (3) apparent thermodynamic equilibration of O, Mg, and Fe between minerals based on the consistency of independent thermometry results. First, detailed petrographic observations using both optical microscopy and backscatter electron imaging demonstrate that all mineral grains in the studied samples are homogeneous (Fig. 2; Fig. 3). Chemical homogeneity within mineral grains is further confirmed by EMPA point analyses along profiles across mineral boundaries (Fig. 3). These attest to the attainment of inter-mineral chemical equilibrium and rule out the possibility that the Fe isotope variations observed between different YBIF samples is caused by chemical diffusion (Dauphas, 2007; Teng et al., 2011) or thermal diffusion (Huang et al., 2010; Richter et al., 2009).

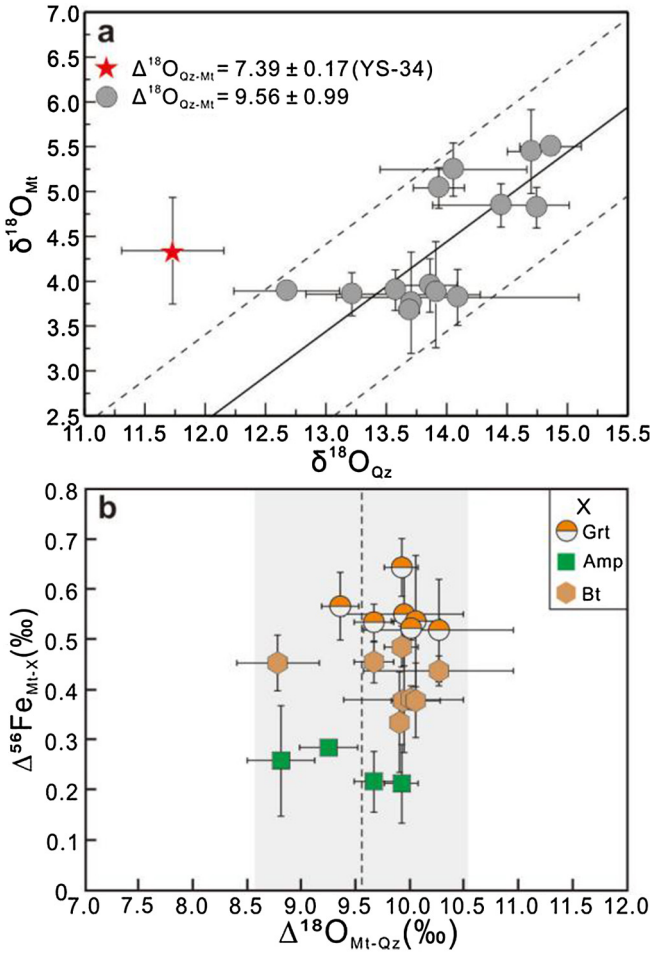

Fig. 5. (a) O isotope composition of quartz (Qz) and magnetite (Mt) from the YBIF. (b) Binary diagram illustrating the $\Delta^{18}O_{Mt\text{-}Qz}$ and $\Delta^{56}Fe_{Mt\text{-}x}$ for Fe-bearing mineral pairs.

Second, despite the large Fe isotope variability in each of the Fe-bearing minerals among the 16 YBIF samples, the offset in δ^{56}Fe between the six mineral pairs does not vary significantly (Fig. 6). This kind of phenomena has been suggested as strong evidence for the attainment of equilibrium isotope fractionation in previous studies (e.g., Anderson et al., 1971; Valley and O'Neil, 1981; Blattner, 1975; Dunn and Valley, 1992; Kitchen and Valley, 1995; Valley et al., 2003; Proskurowski et al., 2006; Williams et al., 2007; Liu et al., 2011; Huang et al., 2011; Quade et al., 2013; Li et al., 2011). Furthermore, the whole-rock Fe isotope composition ($\delta^{56}Fe_{whole\text{-}rock}$; Supplementary Table S4; Fig. S2) calculated based on the δ^{56}Fe of the Fe-bearing minerals and the relative abundance of each mineral measured from μ-XRF mapping is consistent, within analytical error, with the measured $\delta^{56}Fe_{whole\text{-}rock}$ based on whole-rock powders from Ye et al. (2017) (Fig. 4). This consistency indicates that the large variability in δ^{56}Fe for each mineral is the result of re-distribution of Fe isotopes between different minerals that occur in different relative abundances. This requires adequate exchange of Fe between the different Fe-bearing minerals in the YBIF, at least at the scale of a hand specimen (i.e., 10–100 cm). Such complete exchange and re-distribution of Fe isotopes in the samples would result in equilibrium partitioning of Fe isotopes between minerals.

Additionally, the consistency in metamorphic temperatures obtained by magnetite–quartz oxygen isotope thermometry and inter-mineral Fe–Mg exchange thermometry indicates simultaneous attainment of O isotope equilibrium between quartz and magnetite, as well as attainment of Fe and Mg equilibrium among amphibole, garnet, and biotite. The diffusion rates of these three elements in the minerals vary significantly. As shown in Fig. 8, the diffusion rates of Mg in biotite and Fe in magnetite are faster than the diffusion rates for Fe and Mg in garnet, and O in quartz and magnetite. Given that Fe and Mg in garnet had reached equilibrium, Fe must have reached equilibrium in the magnetite–biotite–garnet system. The same concept has been applied to verify the attainment of Sm–Nd–O–Mg isotope equilibrium for samples from Sulu–Dabie orogen, where ultrahigh-pressure metamorphism has been extensively studied (e.g., Zheng et al., 2002, Li et al., 2011).

5.3. Inter-mineral Fe isotope fractionation

The evidence above collectively supports the attainment of Fe isotope equilibrium between magnetite, garnet, amphibole, and biotite at 538 ± 39 °C. According to the theory of isotope distribution (Urey, 1947; Bigeleisen and Mayer, 1947; Schauble, 2004), equilibrium isotope fractionation factors are temperature dependent and can, to a first-order approximation, be described as $10^3 \ln\alpha_{X-Y} = A/T^2$, where T is temperature in Kelvin and A is a constant dependent on the phases considered. Therefore, we can derive the following six temperature-dependent inter-mineral Fe isotope fractionation functions from the four minerals:

$10^3 \ln\alpha_{Mt-Grt} = 0.36(\pm0.05) \times 10^6/T^2$;
$10^3 \ln\alpha_{Mt-Bt} = 0.28(\pm0.07) \times 10^6/T^2$;
$10^3 \ln\alpha_{Mt-Amp} = 0.16(\pm0.04) \times 10^6/T^2$;
$10^3 \ln\alpha_{Amp-Grt} = 0.22(\pm0.10) \times 10^6/T^2$;
$10^3 \ln\alpha_{Amp-Bt} = 0.17(\pm0.03) \times 10^6/T^2$;
and $10^3 \ln\alpha_{Bt-Grt} = 0.09(\pm0.05) \times 10^6/T^2$.

These Fe isotope fractionation functions are internally consistent between the four minerals, despite that the fractionation factors for different mineral pairs are derived from different sample sets. For example, according to the definition of equilibrium isotope fractionation (α), $\alpha_{A-C} = \alpha_{A-B} \times \alpha_{B-C}$, thus $\ln\alpha_{A-C} = \ln\alpha_{A-B} + \ln\alpha_{B-C}$. Such a relationship provides an essential test for the internal consistency of isotope fractionation factors among more than three minerals. The above inter-mineral Fe isotope fractionation functions obtained from the YBIF samples satisfy this test within analytical uncertainties. This further supports the attainment of Fe isotope equilibrium for the samples.

Summarizing the observed Fe isotope data, the degree of heavy Fe isotope enrichment in Fe minerals increases in the order garnet, biotite, amphibole, and magnetite. In general, the bonding environment of cations controls equilibrium isotope fractionation, with heavier isotopes being enriched in minerals with stronger bonds and vice versa (Urey, 1947; Bigeleisen and Mayer, 1947; Schauble, 2004). Minerals in which Fe occurs with lower coordination numbers and higher oxidation states have shorter Fe–O bonds and preferentially incorporate heavy Fe isotopes, whereas minerals in which Fe occurs with higher coordination numbers and lower oxidation states have longer Fe–O bonds and preferentially incorporate light Fe isotopes (e.g., Young et al., 2015). Garnet contains hexagonally coordinated Fe^{2+} ($^{VIII}Fe^{2+}$) and octahedrally coordinated Fe^{3+} ($^{VI}Fe^{3+}$) (Smyth and Bish, 1988), but because of the lower Fe valance ($Fe^{3+}/\sum Fe = 5.4 \pm 2.3\%$), the garnet samples in this study are expected to have dominantly $^{VIII}Fe^{2+}$ and longer Fe–O bonds. By contrast, magnetite contains both tetrahedrally and octahedrally coordinated Fe, and has the highest $Fe^{3+}/\sum Fe$ ratio (66.7%), such that it is expected to have the shortest Fe–O bonds. Iron in amphibole and biotite is octahedrally coordinated (Gunter et al., 2003;

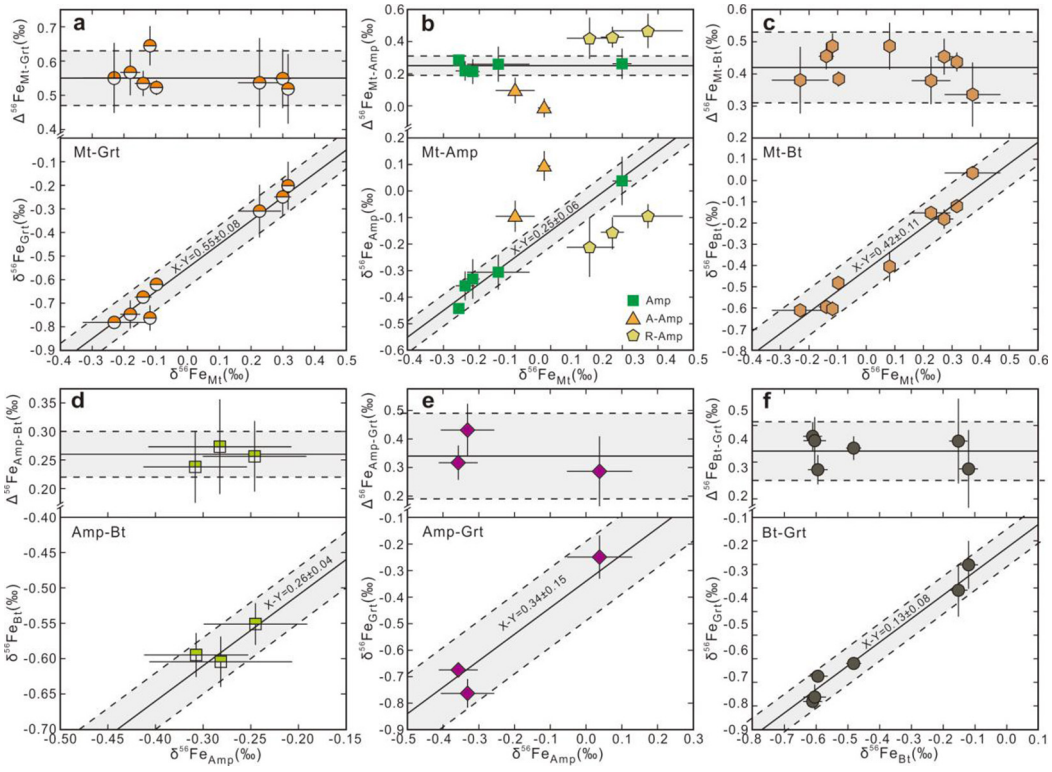

Fig. 6. Cross plots of Fe isotope composition and inter-mineral Fe isotope fractionation factors for mineral pairs. (a) $\Delta^{56}Fe_{Mt-Grt}$ vs. $\delta^{56}Fe_{Mt}$ and $\delta^{56}Fe_{Mt}$ vs. $\delta^{56}Fe_{Grt}$; (b) $\Delta^{56}Fe_{Mt-Amp}$ vs. $\delta^{56}Fe_{Mt}$ and $\delta^{56}Fe_{Mt}$ vs. $\delta^{56}Fe_{Amp}$; (c) $\Delta^{56}Fe_{Mt-Bt}$ vs. $\delta^{56}Fe_{Mt}$ and $\delta^{56}Fe_{Mt}$ vs. $\delta^{56}Fe_{Bt}$; (d) $\Delta^{56}Fe_{Amp-Bt}$ vs. $\delta^{56}Fe_{Amp}$ and $\delta^{56}Fe_{Amp}$ vs. $\delta^{56}Fe_{Bt}$; (e) $\Delta^{56}Fe_{Amp-Grt}$ vs. $\delta^{56}Fe_{Amp}$ and $\delta^{56}Fe_{Amp}$ vs. $\delta^{56}Fe_{Grt}$; (f) $\Delta^{56}Fe_{Bt-Grt}$ vs. $\delta^{56}Fe_{Bt}$ and $\delta^{56}Fe_{Bt}$ vs. $\delta^{56}Fe_{Grt}$. Mt, magnetite; Grt, garnet; Amp, amphibole; A-Amp, Alternation amphibole; R-Amp, Retrograde amphibole; Bt, biotite.

Brookshaw et al., 2014), and so should have Fe–O bond lengths intermediate to garnet and magnetite. Therefore, the observed inter-mineral Fe isotope fractionation relations are consistent with what is expected based on the general theory of isotope fractionation. It should be noted that amphibole is slightly enriched in heavy Fe isotopes over biotite, but the $Fe^{3+}/\sum Fe$ ratio in amphibole (23.6 ± 6.3%) is slightly lower than biotite ($Fe^{3+}/\sum Fe = 29.3$ ± 4.3%) (Fig. 7a). This suggests that, in addition to the oxidation state of Fe, the difference in crystal lattice configuration (i.e., inosilicate versus phyllosilicate) may also affect isotope fractionation.

Equilibrium Fe isotope fractionation between magnetite–garnet has also been experimentally calibrated by Sossi and O'Neil (2017), who reported slightly higher $\Delta^{56}Fe_{Mt-Grt}$ fractionation than that in this study (Fig. 9). Such difference in Fe isotope fractionation is likely controlled by mineral chemistry. The Fe content of garnet (almandine) ($FeO_T = 43.67$ wt.%) synthesized by Sossi and O'Neil (2017) is higher than the Fe content in the garnet ($FeO_T = 31.02$–32.00 wt.%) measured in this study. Additionally, the $Fe^{3+}/\sum Fe$ value of garnet ($Fe^{3+}/\sum Fe = 2.4\%$) in Sossi and O'Neil (2017) is lower than the $Fe^{3+}/\sum Fe$ values of garnet ($3\% \leq Fe^{3+}/\sum Fe \leq 6.4\%$) measured in this study. When the $\Delta^{56}Fe_{Mt-Grt}$ calibrated by Sossi and O'Neil (2017) is extrapolated to 811 K (538 °C) using a $10^3\ln\alpha_{X-Y} = A/T^2$ relation, their data and the data measured in this study define a negative linear trend on a cross-plot of $\Delta^{56}Fe_{Mt-Grt}$ versus Fe^{3+}/Fe_T (Fig. 7b). This indicates that for the same mineralogical group and given the same temperature, the oxidation state of Fe ($Fe^{3+}/\sum Fe$) strongly affects Fe isotope fractionation (e.g., Li et al., 2016; Sossi and O'Neil, 2017).

The Fe-bearing garnet has two end members – Fe(II)-rich almandine and Fe(III)-rich andradite. Based on the linear trend in Fig. 7b, and taking into account the error in regression, a function for the equilibrium Fe isotope fractionation factor between magnetite and garnet is derived:

$$10^3\ln\alpha_{Mt-Grt} = [(-2.4 \pm 0.3) \times (Fe^{3+}/\sum Fe)_{Grt} + 0.5 \pm 0.016] \times 10^6/T^2 \quad (3)$$

This function should more accurately describe the Fe isotope fractionation between magnetite–almandine, where $Fe^{3+}/\sum Fe$ is below 0.1. For the andradite end member of garnet, the uncertainty associated with extrapolation is too large. Future work is required for calibration of Fe isotope fractionation between magnetite and andradite.

5.4. Comparison of $\Delta^{56}Fe_{Mt-Grt}$ derived by theoretical calculation, experimental calibration, and observation of natural samples.

Inter-mineral equilibrium Fe isotope fractionation factors can be theoretically calculated from the reduced partition function ratios (RPFR, or β-factor) of the individual minerals of interest (e.g., Polyakov et al., 2019). Theoretical functions of β-factor are available for garnet based on Mössbauer spectroscopy (Eeckhout and De Grave, 2003), and magnetite based on the Mössbauer spectroscopy (Mineev et al., 2007) or Nuclear Resonant Inelastic X-ray Scattering (NRIXS) (Polyakov et al., 2007; Dauphas et al., 2012; Roskosz et al., 2015). Combining these β-factors, four temperature-dependent functions of $10^3\ln\alpha_{Mt-Grt}$ are calculated and plotted in Fig. 10. The Fe isotope fractionation factors between magnetite and garnet from the experimental study of Sossi and O'Neil (2017) and this study are also plotted for comparison. As shown in Fig. 10, the $10^3\ln\alpha_{Mt-Grt}$ obtained from theoretical calculations based on Mössbauer and NRIXS spectroscopy are in excellent agreement with those obtained by experimental calibration (Sossi and O'Neil, 2017) and observation of natural samples (this study). Such consistency attests to the robustness of the obtained equilibrium $\Delta^{56}Fe_{Mt-Grt}$ fractionation factors, allowing them to be applied confidently in future studies.

6. IMPLICATIONS

6.1. Fe isotopes as a potential geothermometer

Inter-mineral equilibrium isotope fractionation can be applied as a geothermometer if the following requirements are satisfied: (1) the equilibrium isotope fractionation factor is large and well-calibrated, and (2) coexisting minerals commonly occur in nature over a range of physicochemical conditions. Shahar et al. (2008) was the first to propose the fractionation of Fe isotopes between magnetite–fayalite ($10^3\ln\alpha^{57}_{Mt-Fa} = 0.3 \times 10^6/T^2$) as a potential geothermometer. Fayalite, however, is less common compared to the Mg-rich end member forsterite. In this study, the Fe isotope fractionation between magnetite and garnet is large enough to have reasonable temperature sensitivity (i.e., ~1.44‰ at temperatures of 500 K) given the analytical precision of Fe isotope ratios. Moreover, magnetite and garnet are both common rock-forming minerals with wide stability fields, co-existing in a variety of geologic settings from upper mantle to lower crust (Green and Ringwood, 1967; Harlov, 2000), and occurring in many Fe skarn deposits (Meinert et al., 2005; Wang et al., 2011). Our work also constrains the Fe isotope fractionation between magnetite and biotite. Although Fe isotope fractionation for this mineral pair is less significant than for the magnetite–garnet pair (Fig. 9), biotite is a ubiquitous mineral in granitic rocks, making it possible to use inter-mineral Fe isotope fractionation to understand the thermal history of granitic magmatism.

6.2. Fe isotopes as indicators of metasomatic/metamorphic processes

Well-calibrated inter-mineral Fe isotope fractionation factors can also be used to understand the processes that affected metamorphic and igneous rocks. Protracted metamorphism would result in equilibrium isotope distribution between minerals, however, overprinting by retrograde metamorphism or hydrothermal fluids would alter the Fe isotope composition of certain minerals while leaving the others unchanged, causing apparent Fe isotope disequilibrium. This is manifested by the Fe isotope signatures of altered amphiboles (A-Amp and R-Amp). Both chemical

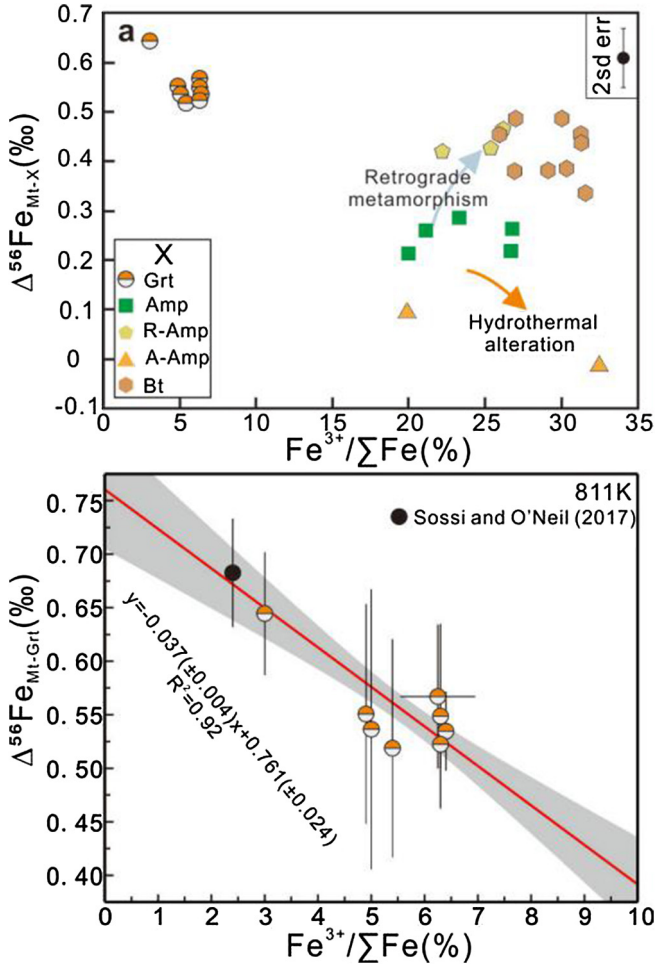

Fig. 7. Binary diagram illustrating the $\Delta^{56}Fe_{Mt\text{-}X}$ and Fe^{3+}/Fe_T for (a) all coexisting Fe-bearing minerals (garnet, R-Amp, Amp, A-Amp and Bt) and (b) garnet. The $\Delta^{56}Fe_{Mt\text{-}Alm}$ data is from Sossi and O'Neil (2017). Note the grey field represents the 95% confidence area for the linear fit. The error of slope for 95% confidence area is reduced (detail in Supplementary Fig. S5).

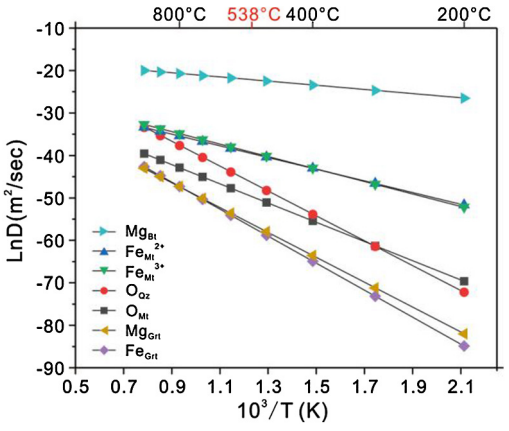

Fig. 8. Diffusion constants of Fe-Mg-O in magnetite, quartz, garnet, amphibole and biotite. Oxygen in quartz (Farver and Yund, 1991), O in magnetite (Gilletti and Hess, 1988), Fe in magnetite (Hallström et al., 2011), Fe and Mg in garnet (Perchuk et al., 2009), and Mg in biotite (Freer, 1981).

(Fig. 2; Supplementary Fig. S3, Fig. S4; Table S3) and Fe isotope (Fig. 4; Fig. 7a; Table 1) compositions of A-Amp and R-Amp were reset. The chemical compositions of A-Amp and R-Amp are similar (Supplementary Fig. S3, Fig. S4), but they record opposite Fe isotope fractionation trends relative to the original amphibole minerals (Fig. 4; Fig. 7a; Table 1), indicative of Fe isotope disequilibrium.

The opposite Fe isotope fractionation trends reflected by $\Delta^{56}Fe_{Mt\text{–}A\text{-}Amp}$ and $\Delta^{56}Fe_{Mt\text{–}R\text{-}Amp}$ (Fig. 7a) suggests a potential connection between the Fe isotope signature of altered minerals and the post-metamorphic process. In a study by Zhu et al. (2018) on altered granites, the $\delta^{56}Fe$ values of altered rocks increased with the degree of K-feldspar alteration. Because hydrothermal fluids are enriched in light Fe isotopes relative to silicate minerals (e.g., Heimann et al., 2008; Wang et al., 2011; Shahar et al., 2008; Sossi and O'Neil, 2017; Zhu et al., 2018), the increase in $\delta^{56}Fe$ values of A-Amp relative to unaltered amphibole is in accord with a hydrothermal origin. It should be noted that the samples that have the highest $\delta^{56}Fe$ value of A-Amp

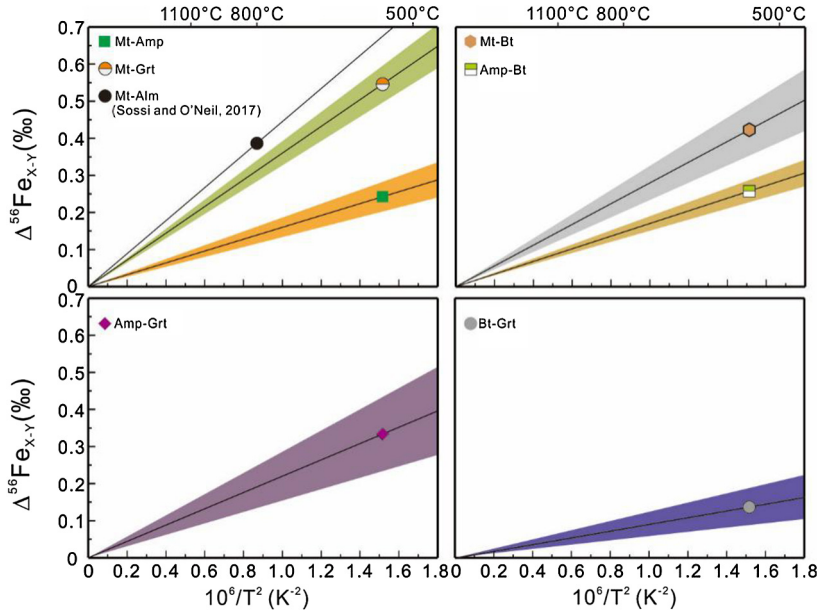

Fig. 9. Equilibrium Fe isotope fractionation factors between (a) magnetite-garnet, magnetite-amphibole, and magnetite-almandine, (b) magnetite-biotite, amphibole-biotite, (c) amphibole-garnet, and (d) biotite-garnet. Mt, magnetite; Grt, garnet; Amp, amphibole; Bt, biotite. The Fe isotope composition of magnetite-almandine is from Sossi and O'Neil (2017).

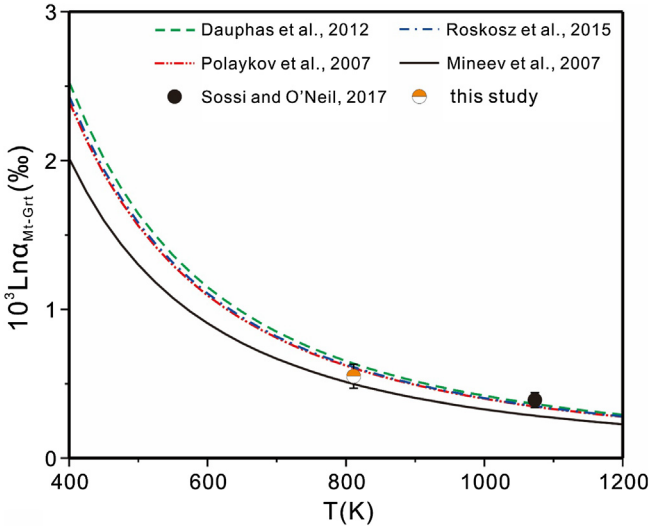

Fig. 10. Comparison of magnetite-garnet Fe isotope fractionation factor from theoretical calculation based on the data of Mössbauer spectroscopy or Nuclear Resonant Inelastic X-ray Scattering (NRIXS) (Eeckhout and De Grave, 2003; Polyakov, 2007; Mineev et al., 2007; Dauphas et al., 2012; Roskosz et al., 2015), experimental calibration (Sossi and O'Neil, 2017) and this study.

also have the lowest $\delta^{18}O_{Qz}$ values (7.39 ± 0.17‰; Table 2). By contrast, the greater value of $\Delta^{56}Fe_{Mineral–R\text{-}Amp}$ relative to $\Delta^{56}Fe_{Mineral–Amp}$ reflects an increase in inter-mineral isotope fractionation with a decrease in temperature during retrograde metamorphic processes (Supplementary Table S5).

7. CONCLUSIONS

In this study, we carried out a systematic investigation of inter-mineral (magnetite–amphibole–biotite–garnet) Fe isotope fractionation based on metamorphosed ironstone samples from the Yingshan banded iron formation (YBIF), South China. The metamorphic temperature of the YBIF was robustly constrained at 538 ± 39 °C using multiple geothermometers. Multiple lines of evidence indicate the attainment of Fe isotope equilibrium between these minerals. Accordingly, we derived internally consistent temperature-dependent Fe isotope fractionation functions between the four minerals, which are: $10^3\ln\alpha_{Mt–Grt} = 0.36 (\pm0.05) \times 10^6/T^2$, $10^3\ln\alpha_{Mt–Bt} = 0.28(\pm0.07) \times 10^6/T^2$, $10^3\ln\alpha_{Mt–Amp} = 0.16(\pm0.04) \times 10^6/T^2$, $10^3\ln\alpha_{Amp–Grt} = 0.22(\pm0.10) \times 10^6/T^2$, $10^3\ln\alpha_{Amp–Bt} = 0.17(\pm0.03) \times 10^6/T^2$ and $10^3\ln\alpha_{Bt–Grt} = 0.09(\pm0.05) \times 10^6/T^2$. Considering the

compositional variability of garnet in this study and the experimental study of Sossi and O'Neil (2017), we further derived a function that describes the effect of Fe oxidation state in almandine garnet on Fe isotope fractionation: $10^3\ln\alpha_{Mt-Grt} = [-2.4 \pm 0.3\times(Fe^{3+}/\sum Fe)_{Grt} + 0.5 \pm 0.016] \times 10^6/T^2$. The inter-mineral Fe isotope fractionation factors calibrated in this study for four common Fe-bearing minerals provide several new geothermometers, and also demonstrate the potential of Fe isotopes in fingerprinting secondary processes that can overprint igneous and metamorphic rocks.

Declaration of Competing Interest

The authors declare that they have no known competing financial interests or personal relationships that could have appeared to influence the work reported in this paper.

ACKNOWLEDGEMENTS

Professor Yongfei Zheng kindly offered support in O isotope analysis in this study and scientific guidance during the writing of this paper. The manuscript benefited from constructive reviews from V.B. Polyakov and two anonymous reviewers. V.B. Polyakov provided the β-factor data for garnet in his review. This study is supported by National Key R&D Plan of China (2018YFC0603703) and National Natural Science Foundation of China (No. 41622301 to WL and No. 41872077 to CZW). HY was supported by the China Scholarship Council (No. 201806190159). HY thanks Yuxuan Wang for scientific discussion, Xiangxian Ma and Wang Xu for assistance with Mössbauer spectroscopy, Chuan Liu for assistance in SEM imaging, Xiaolong Yan and Xing Liu for assistance in ImagePy software, Ben Dang, and Xiaomin Wang for assistance in field sampling, and Dehong Du for assistance in Fe isotope analysis.

APPENDIX A. SUPPLEMENTARY MATERIAL

Supplementary data to this article can be found online at https://doi.org/10.1016/j.gca.2019.12.014.

REFERENCES

Anbar A. D., Jarzecki A. A. and Spiro T. G. (2005) Theoretical investigation of iron isotope fractionation between $Fe(H_2O)_6^{3+}$ and $Fe(H_2O)_6^{2+}$: implications for iron stable isotope geochemistry. *Geochim. Cosmochim. Acta* **69**, 825–837.

Anderson A. T., Clayton R. N. and Mayeda T. K. (1971) Oxygen isotope thermometry of mafic igneous rocks. *J. Geol.* **79**, 715–729.

Beard B. L. and Johnson C. M. (2004) Fe isotope variations in the modern and ancient earth and other planetary bodies. *Rev. Mineral. Geochem.* **55**, 319–357.

Beard B. L., Handler R. M., Scherer M. M., Wu L., Czaja A. D., Heimann A. and Johnson C. M. (2010) Iron isotope fractionation between aqueous ferrous iron and goethite. *Earth Planet. Sci. Lett.* **295**, 241–250.

Becker R. H. and Clayton R. N. (1976) Oxygen isotope study of a Precambrian banded iron-formation, Hamersley Range Western Australia. *Geochim. Cosmochim. Acta* **40**, 1153–1165.

Bigeleisen J. and Mayer M. G. (1947) Calculation of equilibrium constants for isotopic exchange reactions. *J. Chem. Phys.* **15**, 261–267.

Blanchard M., Balan E. and Schauble E. A. (2017) Equilibrium fractionation of non-traditional isotopes: a molecular modeling perspective. *Rev. Mineral. Geochem.* **82**, 27–63.

Blanchard M., Dauphas N., Hu M. Y., Roskosz M., Alp E. E., Golden D. C., Sio C. K., Tissot F. L. H., Zhao J., Gao L., Morris R. V., Fornace M., Floris A., Lazzeri M. and Balan E. (2015) Reduced partition function ratios of iron and oxygen in goethite. *Geochim. Cosmochim. Acta* **151**, 19–33.

Blanchard M., Poitrasson F., Méheut M., Lazzeri M., Mauri F. and Balan E. (2009) Iron isotope fractionation between pyrite (FeS_2), hematite (Fe_2O_3) and siderite ($FeCO_3$): a first-principles density functional theory study. *Geochim. Cosmochim. Acta* **73**, 6565–6578.

Blattner P. (1975) Oxygen isotopic composition of fissure-grown quartz, adularia, and calcite from Broadlands geothermal field, New Zealand. *Am. J. Sci.* **275**, 785–800.

Brookshaw D. R., Lloyd J. R., Vaughan D. J. and Pattrick R. A. D. (2014) Bioreduction of biotite and chlorite by a Shewanella species. *Am. Mineral.* **99**, 1746–1754.

Carswell D. A. and Zhang R. Y. (1999) Petrographic characteristics and metamorphic evolution of ultrahigh-pressure eclogites in plate-collision belts. *Int. Geol. Rev.* **41**, 781–798.

Chiba H., Chacko T., Clayton R. N. and Goldsmith J. R. (1989) Oxygen isotope fractionations involving diopside, forsterite, magnetite, and calcite - application to geothermometry. *Geochim. Cosmochim. Acta* **53**, 2985–2995.

Dauphas N. (2007) Diffusion-driven kinetic isotope effect of Fe and Ni during formation of the Widmanstatten pattern. *Meteorit. Planet. Sci.* **42**, 1597–1613.

Dauphas N., John S. G. and Rouxel O. (2017) Iron isotope systematics. *Rev. Mineral. Geochem.* **82**, 415–510.

Dauphas N., Roskosz M., Alp E. E., Golden D. C., Sio C. K., Tissot F. L. H., Hu M. Y., Zhao J., Gao L. and Morris R. V. (2012) A general moment NRIXS approach to the determination of equilibrium Fe isotopic fractionation factors: application to goethite and jarosite. *Geochim. Cosmochim. Acta* **94**, 254–275.

Dauphas N., Roskosz M., Alp E. E., Neuville D. R., Hu M. Y., Sio C. K., Tissot F. L. H., Zhao J., Tissandiere L., Medard E. and Cordier C. (2014) Magma redox and structural controls on iron isotope variations in Earth's mantle and crust. *Earth Planet. Sci. Lett.* **398**, 127–140.

Domagal-Goldman S. D. and Kubicki J. D. (2008) Density functional theory predictions of equilibrium isotope fractionation of iron due to redox changes and organic complexation. *Geochim. Cosmochim. Acta* **72**, 5201–5216.

Du D. H., Wang X. L., Yang T., Chen X., Li J. Y. and Li W. (2017) Origin of heavy Fe isotope compositions in high-silica igneous rocks: a rhyolite perspective. *Geochim. Cosmochim. Acta* **218**, 58–72.

Dunn S. R. and Valley J. W. (1992) Calcite–graphite isotope thermometry: a test for polymetamorphism in marble, Tudor gabbro aureole, Ontario Canada. *J. Metamorph. Geol.* **10**, 487–501.

Eeckhout S. G. and De Grave E. (2003) Evaluation of ferrous and ferric Mössbauer fractions Part II. *Phys. Chem. Miner* **30**, 142–146.

Farver J. R. and Yund R. A. (1991) Oxygen diffusion in quartz - dependence on temperature and water fugacity. *Chem. Geol.* **90**, 55–70.

Ferry J. M. and Spear F. S. (1978) Experimental calibration of partitioning of Fe and Mg between biotite and garnet. *Contrib. Mineral. Petrol.* **66**, 113–117.

Freer R. (1981) Diffusion in silicate minerals and glasses: a data digest and guide to the literature. *Contrib. Mineral. Petrol.* **76**, 440–454.

Frierdich A. J., Beard B. L., Reddy T. R., Scherer M. M. and Johnson C. M. (2014) Iron isotope fractionation between aqueous Fe(II) and goethite revisited: new insights based on a multi-direction approach to equilibrium and isotopic exchange rate modification. *Geochim. Cosmochim. Acta* **139**, 383–398.

Fujii T., Moynier F., Blichert-Toft J. and Albarède F. (2014) Density functional theory estimation of isotope fractionation of Fe, Ni, Cu, and Zn among species relevant to geochemical and biological environments. *Geochim. Cosmochim. Acta* **140**, 553–576.

Gilletti B. J. and Hess K. C. (1988) Oxygen diffusion in magnetite. *Earth Planet. Sci. Lett.* **89**, 115–122.

Gong B., Zheng Y. F. and Chen R. X. (2007) TC/EA-MS online determination of hydrogen isotope composition and water concentration in eclogitic garnet. *Phys. Chem. Miner.* **34**, 687–698.

Graham C. M. and Powell R. (1984) A garnet hornblende geothermometer - calibration, testing, and application to the pelona schist Southern-California. *J. Metamorph. Geol.* **2**, 13–31.

Green D. H. and Ringwood A. E. (1967) The stability fields od aluminous pyroxene peridotite and garnet peridotite and their relevance in upper mantle structure. *Earth Planet. Sci. Lett* **3**, 151–152.

Gunter M. E., Dyar M. D., Twamley B., Foit F. F. and Cornelius S. (2003) Composition, Fe^{3+}/Sigma Fe, and crystal structure of non-asbestiform and asbestiform amphiboles from Libby, Montana USA. *Am. Mineral.* **88**, 1970–1978.

Hallström S., Hoglund L. and Agren J. (2011) Modeling of iron diffusion in the iron oxides magnetite and hematite with variable stoichiometry. *Acta Mater.* **59**, 53–60.

Harlov D. E. (2000) Titaniferous magnetite-ilmenite thermometry and titaniferous magnetite-ilmenite-orthopyroxene-quartz oxygen barometry in granulite facies gneisses, Bamble Sector, SE Norway: implications for the role of high-grade CO_2- rich fluids during granulite genesis. *Contrib. Mineral. Petrol.* **139**, 180–197.

Heimann A., Beard B. L. and Johnson C. M. (2008) The role of volatile exsolution and sub-solidus fluid/rock interactions in producing high Fe-56/Fe-54 ratios in siliceous igneous rocks. *Geochim. Cosmochim. Acta* **72**, 4379–4396.

Hill P. S. and Schauble E. A. (2008) Modeling the effects of bond environment on equilibrium iron isotope fractionation in ferric aquo-chloro complexes. *Geochim. Cosmochim. Acta* **72**, 1939–1958.

Holdaway M. J. (2000) Application of new experimental and garnet Margules data to the garnet-biotite thermometer. *Am. Mineral.* **85**, 881–892.

Holdaway M. J. and Lee S. M. (1977) Fe-Mg cordierite stability in high-grade pelitic rocks based on experimental, theoretical, and natural observations. *Contrib. Mineral. Petrol.* **63**, 175–198.

Huang F., Chakraborty P., Lundstrom C. C., Holmden C., Glessner J. J. G., Kieffer S. W. and Lesher C. E. (2010) Isotope fractionation in silicate melts by thermal diffusion. *Nature* **464**, 396–400.

Huang F., Zhang Z., Lundstrom C. C. and Zhi X. (2011) Iron and magnesium isotopic compositions of peridotite xenoliths from Eastern China. *Geochim. Cosmochim. Acta* **75**, 3318–3334.

Johnson C. M., Beard B. L. and Roden E. E. (2008) The iron isotope fingerprints of redox and biogeochemical cycling in the modern and ancient Earth. *Annu. Rev. Earth Planet. Sci.* **36**, 457–493.

Kitchen N. E. and Valley J. W. (1995) Carbon isotope thermometry in marbles of the Adirondack Mountains, New York. *J. Metamorph. Geol.* **13**, 577–594.

Krogh E. J. (1988) The garnet-clinopyroxene Fe-Mg geothermometer - a reinterpretation of existing experimental-data. *Contrib. Mineral. Petrol.* **99**, 44–48.

Krogh E. J. and Raheim A. (1978) Temperature and pressure-dependence of Fe-Mg partitioning between garnet and phengite, with particular reference to eclogites. *Contrib. Mineral. Petrol.* **66**, 75–80.

Leake B. E., Woolley A. R., Arps C. E. S., Birch W. D., Gilbert M. C., Grice J. D., Hawthorne F. C., Kato A., Kisch H. J., Krivovichev V. G., Linthout K., Laird J., Mandarino J., Maresch W. V., Nickel E. H., Schumaker J. C., Smith D. C., Stephenson N. C. N., Ungaretti L., Whittaker E. J. W. and Youzhi G. (1997) Nomenclature of amphiboles: report of the subcommittee on amphiboles of the International Mineralogical Association Commission on New Minerals and Mineral Names. *Can. Mineral.* **61**, 295–321.

Li D. Y., Xiao Y. L., Li W. Y., Zhu X., Williams H. M. and Li Y. L. (2016) Iron isotopic systematics of UHP eclogites respond to oxidizing fluid during exhumation. *J. Metamorph. Geol.* **34**, 987–997.

Li W. Y., Teng F. Z., Xiao Y. and Huang J. (2011) High-temperature inter-mineral magnesium isotope fractionation in eclogite from the Dabie orogen China. *Earth Planet. Sci. Lett.* **304**, 224–230.

Li W., Huberty J. M., Beard B. L., Kita N. T., Valley J. W. and Johnson C. M. (2013) Contrasting behavior of oxygen and iron isotopes in banded iron formations revealed by in situ isotopic analysis. *Earth Planet. Sci. Lett.* **384**, 132–143.

Liu J., Dauphas N., Roskosz M., Hu M. Y., Yang H., Bi W., Zhao J., Alp E. E., Hu J. Y. and Lin J. F. (2017) Iron isotopic fractionation between silicate mantle and metallic core at high pressure. *Nat. Commun.* **8**, 14377.

Liu S. A., Teng F. Z., Yang W. and Wu F. Y. (2011) High-temperature inter-mineral magnesium isotope fractionation in mantle xenoliths from the North China craton. *Earth Planet. Sci. Lett.* **308**, 131–140.

Ma X., Zheng G., Sajjad W., Xu W., Fan Q., Zheng J. and Xia Y. (2018) Influence of minerals and iron on natural gases generation during pyrolysis of type-III kerogen. *Mar. Pet. Geol.* **89**, 216–224.

Meinert L.D., Dipple G.M., Nicolescu S. (2005) World skarn deposits: Economic Geology 100th Anniversary Volume, 299−336.

Mineev S. D., Polyakov V. B. and Permyakov Y. V. (2007) Equilibrium iron isotope fractionation factors for magnetite from Mössbauer spectroscopy and inelastic nuclear resonant X-ray scattering data. *Geochim. Cosmochim. Acta* **71**, A669.

O'Neil J. R. (1986) Theoretical and experimental aspects of isotopic fractionation. *Rev. Mineral.* **16**, 1–40.

Ottonello G. and Zuccolini M. V. (2009) Ab-initio structure, energy and stable Fe isotope equilibrium fractionation of some geochemically relevant H-O-Fe complexes. *Geochim. Cosmochim. Acta* **73**, 6447–6469.

Peng X., Chen S. and Xu H. (2013) Formation of biogenic sheath-like Fe oxyhydroxides in a near-neutral pH hot spring: implications for the origin of microfossils in high-temperature, Fe-rich environments. *J. Geophys. Res.: Biogeosci.* **118**, 1397–1413.

Polyakov V. B. (2009) Equilibrium iron isotope fractionation at the core–mantle boundary. *Science* **323**, 912–914.

Polyakov V. B. and Mineev S. D. (2000) The use of Mössbauer spectroscopy in stable isotope geochemistry. *Geochim. Cosmochim. Acta* **64**, 849–865.

Polyakov V. B. and Soultanov D. M. (2011) New data on equilibrium iron isotope fractionation among sulfides: constraints on mechanisms of sulfide formation in hydrothermal and igneous systems. *Geochim. Cosmochim. Acta* **75**, 1957–1974.

Polyakov V. B., Clayton R. N., Horita J. and Mineev S. D. (2007) Equilibrium iron isotope fractionation factors of minerals: reevaluation from the data of nuclear inelastic resonant X-ray scattering and Mossbauer spectroscopy. *Geochim. Cosmochim. Acta* **71**, 3833–3846.

Polyakov V. B., Osadchii E. G., Voronin M. V., Osadchii V. O., Sipavina L. V., Chareev D. A., Tyurin A. V., Gurevich V. M. and Gavrichev K. S. (2019) Iron and sulfur isotope fractors of pyrite: data from experimental Mössbauer spectroscopy and heat capacity. *Geochem. Int.* **57**, 369–383.

Proskurowski G., Lilley M. D., Kelley D. S. and Olson E. J. (2006) Low temperature volatile production at the Lost City Hydrothermal Field, evidence from a hydrogen stable isotope geothermometer. *Chem. Geol.* **229**, 331–343.

Quade J., Eiler J. and Dae M. (2013) The clumped isotope geothermometer in soil and paleosol carbonate. *Geochim. Cosmochim. Acta* **105**, 92–107.

Ravna E. K. (2000) Distribution of Fe^{2+} and Mg between coexisting garnet and hornblende in synthetic and natural systems: an empirical calibration of the garnet-hornblende Fe-Mg geothermometer. *Lithos* **53**, 265–277.

Richter F. M., Dauphas N. and Teng F. Z. (2009) Non-traditional fractionation of non-traditional isotopes: evaporation, chemical diffusion and Soret diffusion. *Chem. Geol.* **258**, 92–103.

Roskosz M., Sio C. K. I., Dauphas N., Bi W., Tissot F. L. H., Hu M. Y., Zhao J. and Alp E. E. (2015) Spinel – olivine – pyroxene equilibrium iron isotopic fractionation and applications to natural peridotites. *Geochim. Cosmochim. Acta* **169**, 184–199.

Rustad J. R. and Dixon D. A. (2009) Prediction of iron-isotope fractionation between hematite (α-Fe_2O_3) and ferric and ferrous iron in aqueous solution from density functional theory. *J. Phys. Chem. A* **113**, 12249–12255.

Schauble E. A. (2004) Applying stable isotope fractionation theory to new systems. *Rev. Mineral. Geochem.* **55**, 65–111.

Schuessler J. A., Schoenberg R., Behrens H. and von Blanckenburg F. (2007) The experimental calibration of the iron isotope fractionation factor between pyrrhotite and peralkaline rhyolitic melt. *Geochim. Cosmochim. Acta* **71**, 417–433.

Shahar, A., Elardo, S. M. and Macris, C. A. (2017) Equilibrium fractionation of non-traditional stable isotopes: an experimental perspective. In: F.Z. Teng, J. Watkins and N. Dauphas (Editors), Non-Traditional Stable Isotopes. Rev. Mineral. Geochem. 82, 65–83.

Shahar A., Schauble E. A., Caracas R., Gleason A. E., Reagan M. M., Xiao Y., Shu J. and Mao W. (2016) Pressure-dependent isotopic composition of iron alloys. *Science* **352**, 580–582.

Shahar A., Young E. D. and Manning C. E. (2008) Equilibrium high-temperature Fe isotope fractionation between fayalite and magnetite: An experimental calibration. *Earth Planet. Sci. Lett.* **268**, 330–338.

Shi Y., Zhu G. and Wang D. (2009) Metamorphic P-T evolution for the garnet amphibolite from Feidong Group in the south of Zhangbaling uplift across Tan-Lu fault and its influence on tectonics. *Acta Petrol. Sinica* **25**, 3335–3345.

Smyth J. R. and Bish D. L. (1988) *Crystal Structures and Cation Sites of the Rock-Forming Minerals*. Allen and Unwin, Boston.

Sossi P. A. and O'Neill H. S. C. (2017) The effect of bonding environment on iron isotope fractionation between minerals at high temperature. *Geochim. Cosmochim. Acta* **196**, 121–143.

Sossi P. A., Foden J. D. and Halverson G. P. (2012) Redox-controlled iron isotope fractionation during magmatic differentiation: an example from the Red Hill intrusion S. Tasmania. *Contrib. Mineral. Petrol.* **164**, 757–772.

Sossi P. A., Nebel O. and Foden J. (2016) Iron isotope systematics in planetary reservoirs. *Earth Planet. Sci. Lett.* **452**, 295–308.

Stookey L. L. (1970) Ferrozine - a new spectrophotometric reagent for iron. *Anal. Chem.* **42**, 779–781.

Teng F. Z., Dauphas N. and Helz R. T. (2008) Iron isotope fractionation during magmatic differentiation in Kilauea Iki Lava Lake. *Science* **320**, 1620–1622.

Teng F. Z., Dauphas N., Helz R. T., Gao S. and Huang S. (2011) Diffusion-driven magnesium and iron isotope fractionation in Hawaiian olivine. *Earth Planet. Sci. Lett.* **308**, 317–324.

Urey H. C. (1947) The thermodynamic properties of isotopic substances. *J. Chem. Soc. (MAY)*, 562–581.

Valley, J. W. (2001) Stable isotope thermometry at high temperatures. In: J.W. Valley and D.R. Cole (Editors), Stable Isotope Geochemistry. Rev. Mineral. Geochem. 365–413.

Valley J. W. and O'Neil J. R. (1981) $^{13}C/^{12}C$ exchange between calcite and graphite: a possible thermometer in Grenville marbles. *Geochim. Cosmochim. Acta* **45**, 411–419.

Valley John W., Bindeman I. N. and Peck W. H. (2003) Empirical calibration of oxygen isotope fractionation in zircon. *Geochim. Cosmochim. Acta* **67**, 3257–3266.

Wang A. L., Yan X. L. and Wei Z. J. (2018) ImagePy: an open-source, Python-based and platform-independent software package for bioimage analysis. *Bioinformatics* **34**, 3238–3240.

Wang Y., Zhu X. K., Mao J. W., Li Z. H. and Cheng Y. B. (2011) Iron isotope fractionation during Skarn-type metallogeny: a case study of Xinqiao Cu-S-Fe-Au deposit in the middle-lower Yangtze Valley. *Ore Geol. Rev.* **43**, 194–202.

Williams L. B., Turner A. and Hervig R. L. (2007) Intracrystalline boron isotope partitioning in illite-smectite: testing the geothermometer. *Am. Mineral.* **92**, 1958–1965.

Yang H., Lin J. F., Hu M. Y., Roskosz M., Bi W., Zhao J. Y., Alp E. E., Liu J., Liu J. C., Wentzowitch R. M., Okuchi T. and Dauphas N. (2019) Iron isotopic fractionation in mineral phases from Earth's lower mantle: did terrestrial magma ocean crystallization fractionate iron isotopes? *Earth Planet Sci. Lett.* **506**, 113–122.

Yardley B. W. D. (1989) *An Introduction to Metamorphic Petrology*. Longman Scientific and Technical/John Wiley & Sons, New York.

Ye, H., Wu, C. Z., Yang, T., Santosh, M., Yao, X. Z., Gao, B. F., Wang, X. L. and Li, W. (2017) Updating the Geologic Barcodes for South China: Discovery of Late Archean Banded Iron Formations in the Yangtze Craton. Sci. Rep. 7.

Young E. D., Manning C. E., Schauble E. A., Shahar A., Macris C. A., Lazar C. and Jordan M. (2015) High-temperature equilibrium isotope fractionation of non-traditional stable isotopes: Experiments, theory, and applications. *Chem. Geol.* **395**, 176–195.

Zhang R. Y., Hirajima T., Banno S., Cong B. and Liou J. G. (1995) Petrology of ultrahigh-pressure rocks from the southern Su-Lu region, eastern china. *J. Metamorph. Geol.* **13**, 659–675.

Zheng Y. F. (1995) Oxygen-isotope fractionation in magnetites - structural effect and oxygen inheritance. *Chem. Geol.* **121**, 309–316.

Zheng Y. F. (2012) Metamorphic chemical geodynamics in continental subduction zones. *Chem. Geol.* **328**, 5–48.

Zheng Y. F., Fu B., Gong B. and Li L. (2003) Stable isotope geochemistry of ultrahigh pressure metamorphic rocks from the Dabie-Sulu orogen in China: implications for geodynamics and fluid regime. *Earth-Sci. Rev.* **62**, 105–161.

Zheng Y. F., Fu B., Li Y. L., Xiao Y. L. and Li S. G. (1998) Oxygen and hydrogen isotope geochemistry of ultrahigh-pressure eclogites from the Dabie Mountains and the Sulu terrane. *Earth Planet. Sci. Lett.* **155**, 113–129.

Zheng Y. F., Wang Z. B., Li S. G. and Zhao Z. F. (2002) Oxygen isotope equilibrium between eclogite minerals and its constraints on mineral Sm-Nd chronometer. *Geochim. Cosmochim. Acta* **66**, 625–634.

Zheng Y. F., Zhao Z. F. and Chen R. X. (2019) Ultrahigh-pressure metamorphic rocks in the Dabie-Sulu orogenic belt: compositional inheritance and metamorphic modification. *Geol. Soc. Spec. Publ.* **474**, 89–132.

Zheng Y. F., Zhou J. B., Wu Y. B. and Xie Z. (2005) Low-grade metamorphic rocks in the Dabie-Sulu orogenic belt: a passive-margin accretionary wedge deformed during continent subduction. *Int. Geol. Rev.* **47**, 851–871.

Zhu Z. Y., Jiang S. Y., Mathur R., Cook N. J., Yang T., Wang M., Ma L. and Ciobanu C. L. (2018) Iron isotope behavior during fluid/rock interaction in K-feldspar alteration zone - a model for pyrite in gold deposits from the Jiaodong Peninsula East China. *Geochim. Cosmochim. Acta* **222**, 94–116.

Associate editor: Fang-Zhen Teng